X-ray magnetic spectroscopy at high pressure: performance of SPring-8 BL39XU

Naomi Kawamura,[a]* Naoki Ishimatsu[b] and Hiroshi Maruyama[b]

[a]Japan Synchrotron Radiation Research Institute (JASRI/SPring-8), 1-1-1 Kouto, Sayo, Hyogo 679-5198, Japan, and [b]Department of Physical Science, Graduate School of Science, Hiroshima University, 1-3-1 Kagamiyama, Higashi-Hiroshima, Hiroshima 739-8526, Japan. E-mail: naochan@spring8.or.jp

An X-ray magnetic circular dichroism experiment under multiple extreme conditions, $2 \leq T \leq 300$ K, $H \leq 10$ T and $P \leq 50$ GPa, has been achieved at SPring-8 BL39XU. A combination of the high-brilliant X-ray beam and a helicity-controlled technique enabled the dichroic signal to be recorded with high accuracy. The performance is shown by the outcome of pressure-induced ferromagnetism in Mn_3GaC and the pressure-suppressed Co moment in $ErCo_2$. Two technical developments, a tiny diamond anvil cell inserted into a superconducting magnet and *in situ* pressure calibration using $90°$ Bragg diffraction from a NaCl marker, are also presented. X-ray magnetic spectroscopy under multiple extreme conditions is now opening a new approach to materials science.

1. Introduction

The extreme conditions used to perturb the electronic and magnetic states of magnetic materials provide important insights into the nature of excited states in interesting magnetic phase transitions. In order to study their structural and electronic responses, pressure is an effective external field for providing a strong influence on such properties at the electronic energy level, as are temperature and magnetic field (Grey & Butler, 2001). The applied pressure induces a contraction in the coordination environment, which results in a decrease in the interatomic distance and affects the symmetry of the crystal structure. Consequently, pressure will give rise to some observable changes in the electronic structure because the local environment is strongly modified. Various pressure-induced phenomena, *e.g.* high-spin–low-spin transition, magnetovolume effect, metal–insulator transition, mixed-valence states, and so on, are some of the intriguing subjects in this field.

In magnetic spectroscopy, X-ray magnetic circular dichroism (XMCD) is a powerful tool for studying the magnetic states in strongly correlated electron systems (Schütz *et al.*, 1987; Chen *et al.*, 1990; Koide *et al.*, 1991). Because XMCD is based on X-ray absorption spectroscopy (XAS), it provides element-selective and electronic-shell-specific information about constituent atoms. In addition, spectroscopic studies under extreme conditions are essential for a deeper understanding of material properties. In the hard X-ray region, a diamond anvil cell (DAC) has been used practically for XAS experiments under high pressure and has also been widely applied to XMCD studies of the K-edge ($1s \rightarrow 4p$ transition) of transition metals (TM), $L_{2,3}$-edges ($2p \rightarrow 5d$ transitions) of rare-earth elements (RE) and noble metals (Odin *et al.*, 1998, 2000; Ishimatsu *et al.*, 2003, 2007*a,b*; Mathon *et al.*, 2004; Haskel *et al.*, 2007). Furthermore, it is relatively easy for a DAC to be specialized for spectroscopy under multiple extreme conditions. The dichroic spectrum originates in the delocalized $4p$ or $5d$ electronic states hybridized with the localized $3d$ or $4f$ states, so that the spectral intensity is, in general, very weak compared with that at the TM $L_{2,3}$-edges ($2p \rightarrow 3d$) and RE $M_{4,5}$-edges ($3d \rightarrow 4f$) in the soft X-ray region. However, for an experiment under high pressure, it is not feasible to perform an XMCD study in the soft X-ray region because of the tremendous absorption by the cell windows.

In order to perform magnetic spectroscopy, beamline 39XU at SPring-8 has been devoted to XMCD experiments in the hard X-ray region (Maruyama *et al.*, 1999). The combination of the high-brilliant beam of a third-generation synchrotron radiation source with a helicity-controlled technique using $\lambda/4$ wave plate enabled us to record the dichroic signal with high accuracy in the wide energy range 5–16 keV. In particular, even a weak dichroic signal with a value of less than 10^{-4} of the normalized XAS spectrum can be observed using the

helicity-modulation technique (Suzuki *et al.*, 1998). Now the XMCD experiment can be expanded to magnetic spectroscopy under multiple extreme conditions.

This paper presents the capabilities of the high-pressure XMCD developed on BL39XU of SPring-8. The X-ray optics and experimental instruments are briefly described in §2.1 and §2.2. For an experiment under high pressure, it is important to monitor the pressure generated inside the sample room of the DAC. Therefore, in addition to the ruby fluorescence method, we have developed an *in situ* pressure calibration method that uses the 90° Bragg diffraction from a NaCl pressure marker, which is advantageous for measurements at low temperatures, as shown in §2.3. §3 is devoted to the outcome of research on pressure-induced ferromagnetism in antiperovskite Mn_3GaC and the pressure-suppressed Co moment in Laves phase $ErCo_2$ (Ishimatsu *et al.*, 2007*b*).

2. SPring-8 BL39XU

2.1. Beamline optics

Fig. 1 shows the layout for the general set-up of the XMCD experiment on BL39XU. X-rays emitted from a linear undulator (Kitamura, 2000) are monochromated by a diamond 111 double-crystal monochromator (DDM) (Yabashi *et al.*, 2007) and converted into a circularly polarized beam using a diamond X-ray phase retarder (XPR) (Hirano *et al.*, 1991). X-rays with a degree of circular polarization, $P_c > 0.9$, are available in the energy range 5–16 keV using diamond slabs of six different thicknesses, 0.34–4.7 mm. A Rh-coated mirror functions as a higher harmonics rejector, and an X-ray beam of 600 µm × 600 µm (FWHM) is led to the sample position. For high-pressure experiments, the X-ray beam is vertically clipped to 50–100 µm by a four-dimensional slit and horizontally focused to 50 µm by a bending cylindrical mirror. The incident flux is estimated to be about 2×10^{11} photons s^{-1} at around 7.7 keV. The optics properties of BL39XU are summarized in Table 1.

In order to record the spectrum with high accuracy, X-ray beam stability and good energy resolution are important in addition to the helicity-modulation method (Suzuki *et al.*, 1998). The SPring-8 synchrotron radiation source has excel-

Table 1
Optics properties of SPring-8 BL39XU.

|	
Energy (keV)	5–38 / 5–16†
Photon flux (photons s^{-1})	1.3×10^{13} at 10 keV
Beam size (FWHM) (µm)	600 (vertical) × 600 / 50‡ (horizontal)
Energy resolution $\Delta E/E$	$< 1 \times 10^{-4}$
Polarization rate	Horizontally linear: $P_L^H > 0.99$
	Vertically linear: $P_L^V > 0.7$–0.9†
	Circular: $P_C > 0.9$†
Higher harmonics contents	higher / fundamental $< 10^{-4}$§

† Using an X-ray phase retarder with applicable thickness. ‡ Using a bent mirror. § Using a Rh-coated mirror.

lent electron orbital position stability (Tanaka *et al.*, 2006); the monochromated X-ray beam is well stabilized owing to the good thermal conductivity of the DDM (Yabashi *et al.*, 2007) and the top-up injection of the synchrotron radiation (Tanaka *et al.*, 2006). This condition enables a long-time or repetitive measurement. In addition, the X-ray beam not only has a high photon flux density but also a better energy resolution of $\Delta E/E < 1 \times 10^{-4}$. This better energy resolution also guarantees a higher P_c converted by XPR. For acquisition of the dichroic signal data, two ionization chambers are placed before and after the sample in transmission mode.

For a single crystal or dilute system, the fluorescence method is also used for XMCD measurement, in which a silicon-drift-detector (SDD) is widely employed. In this case, however, the helicity-modulation technique is not possible because the SDD is a pulse-counting detector, so that XMCD should be recorded in helicity-reversal mode. In order to improve the statistical accuracy, a four-channel SDD with an acceptance area of 40 mm^2 in total (XFlash QUAD 4040, BRUKER AXS) is applied to the fluorescent X-ray measurement. Because of the high counting rate of 4×700000 counts s^{-1} at maximum, the accumulation time is significantly reduced and the dichroic signal of $\sim 5 \times 10^{-3}$ can be clearly recorded using the fluorescent method (Okane *et al.*, 2009).

2.2. DAC, magnet and cryostat

In order to apply high pressure to the magnetic materials, DACs of two different types have been installed for the
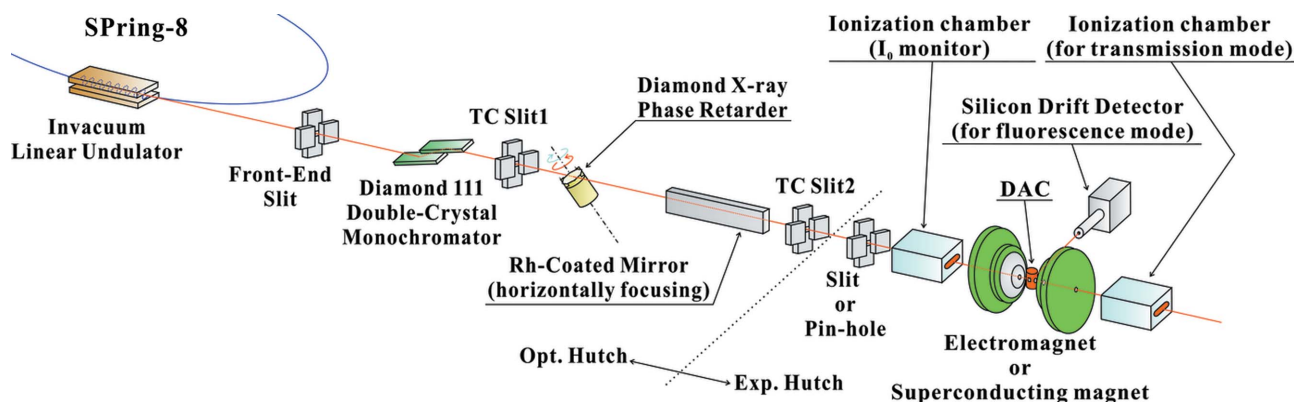
Figure 1
Layout of the general set-up for the XMCD experiment at SPring-8 BL39XU.

XMCD experiment: one is a metal-membrane-driven type (model DXR-GM) and the other is a screw-driven type (tiny-DAC, model cryoDAC-Tesla). Both DACs are made of Cu–Be alloy (easyLab Technologies). The DXR-GM type DAC is mounted on the cold-head of a 4 K GM-cycle cryocooler (Sumitomo Heavy Industry), which is connected to a He-gas charger, allowing the metal-membrane to be controlled *via* a SUS capillary. The generated pressure can be steadily maintained by controlling the He-gas pressure. This system is practical for pressure-dependent XMCD measurements at low temperatures by means of *in situ* regulation of the applied pressure. However, its use is restricted to the case of a low magnetic field, ≤ 0.4 T, by using an electromagnet (EM). To remove this restriction, the tiny-DAC (24 mm in diameter and 47 mm in height) was designed to be inserted into a sample room of a superconducting magnet (SCM, model He-recondensed-type Spectromag, Oxford Instruments).

The XMCD experiment under multiple extreme conditions, $T \geq 2$ K, $H \leq \pm 10$ T and $P \leq 20$ GPa, was conducted using the combination of the tiny-DAC and the SCM. When the temperature cooled from 300 K to 5 K, the pressure decrease was estimated to be 0.1–0.2 GPa. Recently, we manufactured a dual in-line tiny-DAC, which allows us to take measurements for two different samples under the same conditions. These are the most outstanding characteristics of BL39XU at SPring-8. The available experimental conditions for the XMCD measurements are summarized in Table 2. For the low-temperature measurements, the DXR-GM cell is limited to use up to a maximum of 10–20 GPa because downsizing of both X-ray beam and sample area is impeded by a reciprocating vibration of the cryocooler.

For the high-pressure experiments, the thicknesses of two opposing diamond anvils is a crucial problem because the X-ray transmissivity of diamond drastically decreases at X-ray energies below 10 keV. We usually adopt a pair of thin anvils, 1.0 mm in thickness, to reduce the X-ray attenuation. Using these anvils, the X-ray flux transmitted through the DAC accounting for the sample and pressure medium is 4×10^8 photons s^{-1} at the Fe K-edge (beam size of 50 µm $\times$ 50 µm), and a pressure of $\sim$50 GPa has been successfully generated in the case of a culet of diameter 0.35 mm (Ishimatsu *et al.*, 2007a). To extend to the lower photon energy below 7 keV, a perforated diamond anvil with an inner wall of thickness 0.2 mm was tested (Dadashev *et al.*, 2001). As a result, the XAS spectrum of Ce compounds was successfully measured at the Ce L_3-edge.

2.3. *In situ* pressure calibration

For high-pressure experiments, it is necessary to monitor the pressure generated inside the DAC and to regulate the applied pressure. We employed two methods for pressure monitoring: X-ray 90° Bragg diffraction from a NaCl pressure marker (Ishimatsu *et al.*, 2005) and the standard ruby fluorescence method.

Intrinsically, π-polarized X-rays are not horizontally scattered in the 90° direction because of the polarization factor,

Table 2
Available experimental conditions for high-pressure XMCD measurements of BL39XU.

Magnet	Magnetic field (T)	Temperature (K)	Pressure (GPa)	DAC
EM	0.6	11–330	20	Tiny
	0.6	300	50	DXR-GM
	0.4	10–300	10	DXR-GM
SCM	10	2–330	20	Tiny

whereas 90° diffraction occurs for σ-polarized X-rays. On BL39XU, we can use the vertically linearly polarized (σ-polarization) or circularly polarized X-rays converted by the XPR. This conversion is easily performed by controlling the XPR. Therefore, the 90° diffraction method was developed for the XMCD experiment using the split-type SCM, in which the incident and diffracted X-rays penetrate the four-sided Be window of the SCM. In this case, to take out the diffracted X-rays, a Be disc is used as a gasket for the DAC. X-rays diffracted by the NaCl powder are monitored using a NaI scintillation counter fixed at the position $2\theta_B \simeq 90°$. In practice, NaCl 422 and 442 reflections are convenient for observing the Bragg peak by energy scanning in the range 5–10 keV. From the thus determined lattice parameter of NaCl, the pressure is evaluated using Decker's equation of state (Decker, 1971; Onodera *et al.*, 1987). For the diffraction, the X-ray beam size is almost the same as the cross section of the DAC sample room so as to monitor the weak intensity diffracted from NaCl powder. Therefore, this method is insensitive to the pressure distribution inside the sample room, and the estimated pressure is regarded as an average value with an accuracy of ± 0.1 GPa. Fig. 2 shows an example of the 90° diffraction from the NaCl 422 reflection at 0.9 GPa at 258 K. The Bragg peak is observed at 7.600 keV by energy scanning. The peak position shifts to the higher-energy side with decreasing temperature or increasing pressure because of the contraction of the lattice constant. This method is practical for the range below 10 GPa; however, it is difficult to use at the higher pressures owing to broadening of the X-ray diffraction profile.
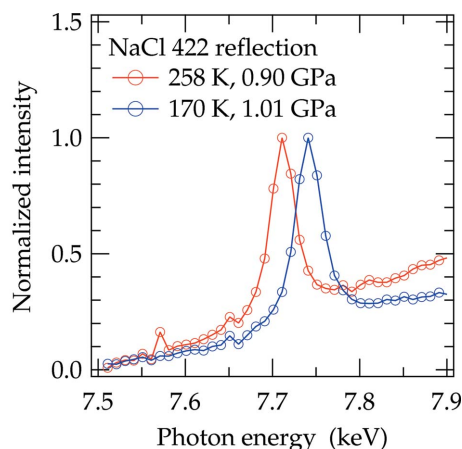
Figure 2
NaCl 422 Bragg reflection under the fixed condition of $2\theta_B = 91.68°$.

The standard ruby fluorescence method is also employed for pressure monitoring. In particular, for the pressure-dependent XMCD at low temperatures, this method is useful for making *in situ* measurements of the pressure generated inside the built-in DAC of the cryocooler. At BL39XU, the monitoring system is installed in the experimental station neighbouring the XMCD apparatus and is suited to an optical cryostat, such as a He-gas flowing-type (HF-cryo) or a closed-cycle refrigerator.

3. XMCD at high pressure

For itinerant electron magnetism, the magnetic interaction is strongly correlated with the conduction electrons hybridized with magnetic localized electrons, such as 3*d*, 4*f* and 5*f* electrons. Pressure directly gives a strong electronic hybridization on the itinerant electron system, so that various pressure-induced phenomena are observed as macroscopic properties. To investigate the itinerant electron magnetism from a microscopic viewpoint, XMCD under multiple extreme conditions was realised by adapting a tiny-DAC to the EM or SCM. Here, two typical topics, *i.e.* the pressure-induced magnetic phase transition in Mn_3GaC and the reduction of the Co magnetic moment in $ErCo_2$ at high pressure, are briefly introduced as application examples of the tiny-DAC.

3.1. Pressure-induced magnetic phase transition in Mn_3GaC

For Mn alloys and compounds in an itinerant electron system, the occurrence of ferromagnetic ordering is closely associated with the Mn—Mn interatomic distance (Kanomata *et al.*, 1987). Antiperovskite Mn_3GaC shows a variety of phase transitions, which may be ascribed to electronic states that sensitively depend on external fields: temperature, magnetic field and pressure (Fruchart & Bertaut, 1978; Kaneko *et al.*, 1987). At ambient pressure (AP), a decrease in temperature gives rise to a transition from the paramagnetic to ferromagnetic (F) phase at T_c = 248 K and successively another one from F to an antiferromagnetic (AF) phase at T_t = 168 K. From the pressure dependence of the magnetization, T_c slightly increases, whereas T_t decreases under applied pressure up to 1.5 GPa (Kamishima *et al.*, 1998, 2002). Therefore, the temperature region of the F-phase is expanded and the F-state is stabilized by applying pressure. In the previous experiment, however, the applied pressure was restricted to 1.5 GPa or less. To examine the stabilized F-state at much higher pressure, we have studied the XMCD under high pressure at room temperature. As a result, a pressure-induced F-phase has been discovered in the range 5–30 GPa (Kawamura *et al.*, 2005). To investigate the stability of the F-state in detail, we aimed to measure the XMCD spectrum under high pressure at a low temperature of around T_t for the F–AF transition. For this purpose, the HF-cryo with the built-in tiny-DAC fulfilled its function.

Fig. 3 shows the XAS and XMCD spectra at the Ga K-edge at 20 K and 8.8 GPa compared with those at AP. The XAS spectrum consists of two moderate peaks, which shift
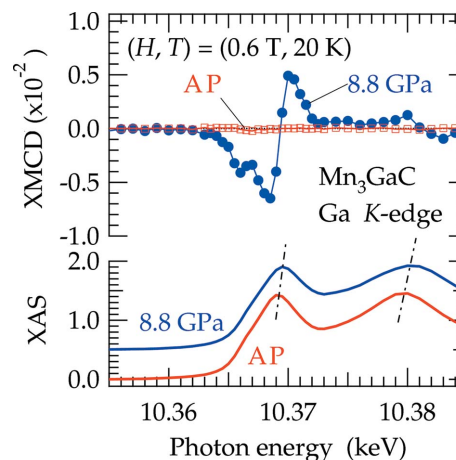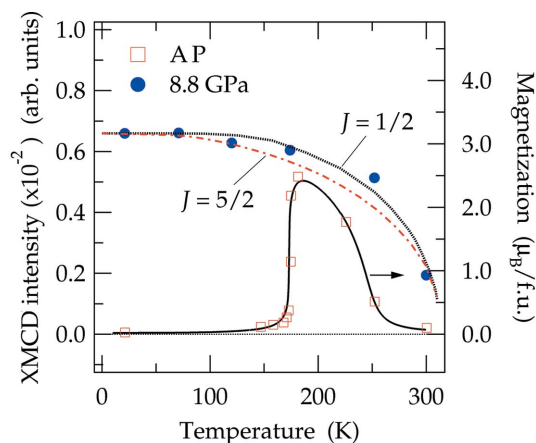

Figure 3
XAS and XMCD spectra at the Ga K-edge in Mn_3GaC. The results between AP (open squares) and 8.8 GPa (solid circles) are compared at 20 K and 0.6 T.

to the higher-energy side according to Natoli's relation: $\mathbf{k} \cdot \mathbf{r}$ = constant (Natoli, 1983). No change is observed in the XAS profile between 8.8 GPa and AP. Therefore, the crystal structure is maintained, except for the contraction of the lattice constant. The XMCD signal is absent at AP owing to the AF-state at 20 K, while the dispersion-type dichroic profile is clearly observed at 8.8 GPa. These findings show that the F-state in Mn_3GaC is induced by applying pressure, that is, the pressure-induced ferromagnetism is also stabilized at low temperatures. The spectral profile is very similar to that observed in the F-state in the range 170–250 K at AP (Kawamura *et al.*, 2007); however, the dichroic intensity is enhanced by pressure. This result suggests that the Ga 4*p*-polarized states are caused by the neighbouring Mn atoms and are affected by a decrease in the Ga—Mn distance. Under high pressure, the Mn 3*d*-states are more hybridized with *p*-symmetric orbitals on the neighbouring sites. The Ga 4*p*-polarized states may be regarded as a good index of the Mn 3*d* magnetic polarization.

Thermal perturbation is also crucial for understanding the pressure-induced F-phase in Mn_3GaC. Therefore, we measured the temperature-dependent XMCD spectrum at 8.8 GPa. Fig. 4 shows the dichroic intensity as a function of temperature. When the temperature increases, the intensity gradually decreases along a convex curve based on the Weiss theory. This behaviour is quite different from the result at AP, that is, the AF-state under pressure is no longer stable at low temperatures. Furthermore, one can discover not only the disappearance of T_t but also an increase of T_c. On the assumption that the Ga K-edge XMCD intensity could be proportional to the spontaneous magnetization, the temperature dependence is explained well by a Brillouin function, in which the behaviour is favourable to the case of J = 1/2 rather than J = 5/2. This result indicates that the Mn magnetic moment is $\sim$1 μ_B in the pressure-induced F-phase, and the value is almost the same as that of the metamagnetic phase induced by a high magnetic field of over 20 T (Kamishima *et al.*, 1998). The occurrence of a small Mn

Figure 4
Temperature dependence of the XMCD intensity at 0.6 T as a comparison of 8.8 GPa (solid circles) with AP (open squares). The magnetization dependent on temperature at 0.6 T and AP is also shown (solid line). Dotted and dashed lines represent spontaneous magnetization curves for $J = 1/2$ and $5/2$, respectively, which are calculated by the classical molecular field theory.

magnetic moment in the pressure-induced or field-induced F-state could be explained by the large spin fluctuations.

Consequently, the XMCD technique offers a competent method for studying magnetism under extremely high pressure, compared with the conventional measurement techniques, such as VSM or SQUID. For an itinerant electron system, the P–T phase diagram can be expanded to a higher-pressure region using so-called XMCD magnetometry.

3.2. Reduction of the Co magnetic moment in ErCo$_2$ at high pressure

Laves phase compounds, RE-Co$_2$, are regarded as model materials for itinerant electron metamagnetism (IEM). It has been explained that Co $3d$ states are located near the critical conditions for stabilizing the Co moment (Wohlfarth & Rhodes, 1962), and that the Co sublattice is magnetically ordered by a large molecular field owing to RE moments (Bloch *et al.*, 1975; Herrero-Albillos *et al.*, 2008). Among them, ErCo$_2$ shows a first-order phase transition from a paramagnetic to ferrimagnetic state at $T_c = 32$ K and $P = $ AP (Bartashevich *et al.*, 1997). As the pressure increases up to $P_t = 2.5$ GPa, T_c decreases linearly to about 13 K, and the phase transition changes from first order to second order above P_t (Hauser *et al.*, 1998; Syshchenko *et al.*, 2001). The effect of pressure has been interpreted as a decrease in the influence of the molecular field on the Co moment. Consequently, it has been predicted that the Co moment mostly disappears above P_t while the Er moment is not modified by the applied pressure. In order to obtain experimental evidence of the pressure dependence of both the Er and Co magnetic states, we made XMCD measurements at the Co K-edge and Er $L_{2,3}$-edges under multiple extreme conditions ($H = 5$ T, $T = 5$ K and P up to 4.2 GPa) by using the tiny-DAC with the SCM (Ishimatsu *et al.*, 2007b).

Fig. 5 shows the XMCD spectra at the Co K-edge and Er $L_{2,3}$-edges. As the pressure increases, the Co K-edge XMCD amplitude becomes small at $P = 2.0$ GPa, and the dichroic profile drastically changes at $P \geq 3.2$ GPa (see Fig. 5a). These changes include an RE contribution to the Co moment (Chaboy *et al.*, 1996; Laguna-Marco *et al.*, 2005); the reduction of the amplitude indicates that the effect of Er on the Co $4p$ states is progressively softened owing to weak mixing between the Co and Er conduction electrons. Moreover, the change in the spectral profile at $P \geq 3.2$ GPa is explained by a significant reduction in the influence of the Er moment. The result is in
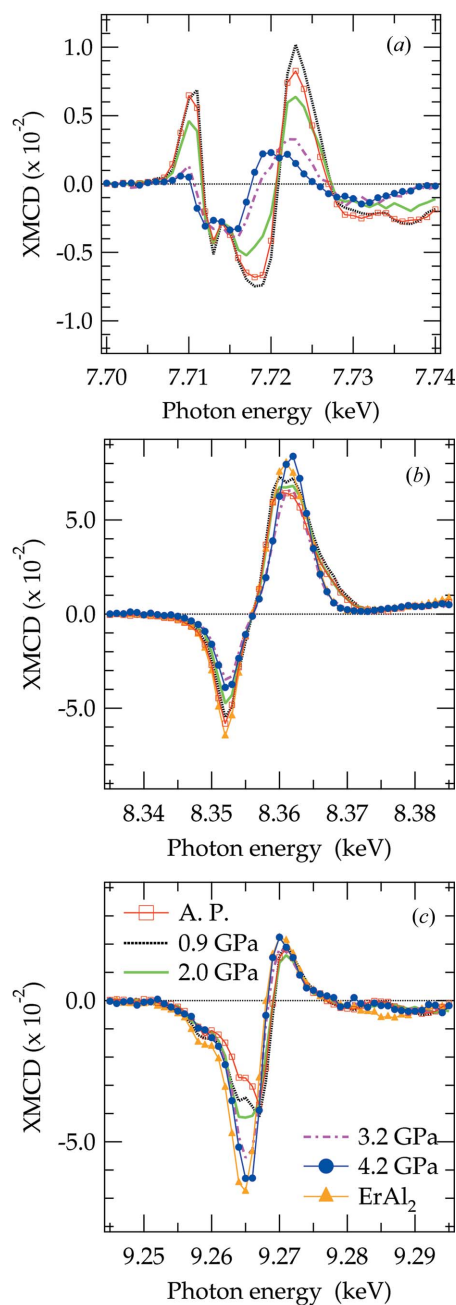
Figure 5
XMCD spectra at the (*a*) Co K-edge, (*b*) Er L_3-edge and (*c*) Er L_2-edge at various pressures. For Er L-edges, the XMCD spectrum of ErAl$_2$ at AP is shown for comparison.

agreement with the previous interpretation; the RE–Co–RE exchange interaction becomes less effective in inducing the IEM as the effect of the molecular field is counteracted by the applied pressure (Syshchenko *et al.*, 2001).

From the dichroic spectra at the Er $L_{2,3}$-edges, the pressure dependence of the Er and Co moments was also examined. When the pressure increases, the L_2-edge spectrum shows an increase in dichroic intensity, whereas the L_3-edge profile presents a small variation, as shown in Figs. 5(b) and 5(c). We supposed that the Co contribution to the Er L-edges XMCD could be extracted from the difference between the spectra for $ErCo_2$ and $ErAl_2$. As seen in Fig. 5(b), a major difference appears in the part of the negative peak in the L_2-edge spectrum. The intensity of this difference linearly decreases with increasing pressure, which suggests that the Co contribution is suppressed by applied pressure. On the assumption that the difference in intensity is proportional to the magnitude of the Co moment, the Co moment linearly decreases with increasing pressure and would disappear at around 5 GPa. On the other hand, the L_3-edge spectrum shows only a weak variation with the applied pressure. This behaviour indicates that the Er moment almost maintains its original magnitude, even under high pressure.

The present experiment proves that the Co and Er components of $ErCo_2$ show different responses to the applied pressure. This phenomenon may be ascribed to the unstable Co moment resulting from the decrease in the effect of the molecular field by the Er moments. This study demonstrates that the element selectivity of XMCD and its performance under multiple extreme conditions will contribute to a fuller understanding of the magnetic phase transition in itinerant electron systems.

4. Summary

Multiple extreme conditions, *i.e.* low temperature, high magnetic field and high pressure, were realised to develop XMCD experiments. The combination of stable X-ray optics with the helicity-modulation technique provided us with a dichroic spectrum with a high precision of better than 10^{-4}. Moreover, *in situ* methods for pressure calibration were established. Circularly polarized X-rays in the wide energy range 5–16 keV and multiple extreme conditions offer important insights into magnetic elements for materials science from the microscopic viewpoint.

References

Bartashevich, M. I., Katori, H. A., Goto, T., Wada, H., Maeda, T., Mori, T. & Shiga, M. (1997). *Physica B*, **229**, 315–320.

Bloch, D., Edwards, D. M., Shimizu, M. & Voiron, J. (1975). *J. Phys. F*, **5**, 1217–1226.

Chaboy, J., Maruyama, H., García, L. M., Bartolomé, J., Kobayashi, K., Kawamura, N., Marcelli, A. & Bozukov, L. (1996). *Phys. Rev. B*, **54**, R15637–R15640.

Chen, C. T., Sette, F., Ma, Y. & Modesti, S. (1990). *Phys. Rev. B*, **42**, 7262–7265.

Dadashev, A., Pasternak, M. P., Rozenberg, G. Kh. & Taylor, R. D. (2001). *Rev. Sci. Instrum.* **72**, 2633–2637.

Decker, D. L. (1971). *J. Appl. Phys.* **42**, 3239–3244.

Fruchart, D. & Bertaut, E. F. (1978). *J. Phys. Soc. Jpn*, **44**, 781–791.

Grey, J. K. & Butler, I. S. (2001). *Coord. Chem. Rev.* **219–221**, 713–759.

Haskel, D., Tseng, Y. C., Lang, J. C. & Sinogeikin, S. (2007). *Rev. Sci. Instrum.* **78**, 083904.

Hauser, R., Bauer, E. & Gratz, E. (1998). *Phys. Rev. B*, **57**, 2904–2914.

Herrero-Albillos, J., Paudyal, D., Bartolomé, F., García, L. M., Pecharsky, V. K., Gschneidner, K. A. Jr, Young, A. T., Jauen, N. & Rogalev, A. (2008). *J. Appl. Phys.* **103**, 07E146.

Hirano, K., Izumi, K., Ishikawa, T., Annaka, S. & Kikuta, S. (1991). *Jpn. J. Appl. Phys.* **30**, L407–L410.

Ishimatsu, N., Maruyama, H., Kawamura, N., Ohishi, Y. & Shimomura, O. (2005). *Nucl. Instrum. Methods Phys. Res. B*, **238**, 167–170.

Ishimatsu, N., Maruyama, H., Kawamura, N., Suzuki, M., Ohishi, Y., Ito, M., Nasu, S., Kawakami, T. & Shimomura, O. (2003). *J. Phys. Soc. Jpn*, **72**, 2372–2376.

Ishimatsu, N., Maruyama, H., Kawamura, N., Suzuki, M., Ohishi, Y. & Shimomura, O. (2007a). *J. Phys. Soc. Jpn*, **76**, 064703.

Ishimatsu, N., Miyamoto, S., Maruyama, H., Chaboy, J., Laguna-Marco, M. A. & Kawamura, N. (2007b). *Phys. Rev. B*, **75**, 180402.

Kamishima, K., Bartashevich, M. I., Goto, T., Kikuchi, M. & Kanomata, T. (1998). *J. Phys. Soc. Jpn*, **67**, 1748–1754.

Kamishima, K., Goto, T., Sasaki, T., Kanomata, T. & Inami, T. (2002). *J. Phys. Soc. Jpn*, **71**, 922–926.

Kaneko, T., Kanomata, T. & Shirakawa, K. (1987). *J. Phys. Soc. Jpn*, **56**, 4047–4055.

Kanomata, T., Shirakawa, K. & Kaneko, T. (1987). *J. Magn. Magn. Mater.* **65**, 76–82.

Kawamura, N., Ishimatsu, N., Isshiki, M., Komatsu, Y. & Maruyama, H. (2005). *Phys. Scr.* T**115**, 591–593.

Kawamura, N., Maruyama, H., Suzuki, M. & Ishikawa, T. (2007). *J. Phys. Soc. Jpn*, **76**, 074716.

Kitamura, H. (2000). *J. Synchrotron Rad.* **7**, 121–130.

Koide, T., Shidara, T., Yuri, M., Kandaka, N. & Fukutani, H. (1991). *Appl. Phys. Lett.* **58**, 2592–2594.

Laguna-Marco, M. A., Chaboy, J. & Maruyama, H. (2005). *Phys. Rev. B*, **72**, 094408.

Maruyama, H., Suzuki, M., Kawamura, N., Ito, M., Arakawa, E., Kokubun, J., Hirano, K., Horie, K., Uemura, S., Hagiwara, K., Mizumaki, M., Goto, S., Kitamura, H., Namikawa, K. & Ishikawa, T. (1999). *J. Synchrotron Rad.* **6**, 1133–1137.

Mathon, O., Baudelet, F., Itié, J. P., Polian, A., d'Astuto, M., Chervin, J. C. & Pacarelli, S. (2004). *Phys. Rev. Lett.* **93**, 255503.

Natoli, C. R. (1983). *EXAFS and Near Edge Structure, Springer Series in Chemical Physics*, Vol. 27, edited by A. Bianconi, L. Incoccia and S. Stipcich, p. 43. Berlin: Springer.

Odin, S., Baudelet, F., Dartyge, E., Ité, J. P., Polian, A., Chervin, J. C., Kappler, J. P., Fontaine, A. & Pizzini, S. (2000). *Philos. Mag. B*, **80**, 155–163.

Odin, S., Baudelet, F., Ité, J. P., Polian, A., Pizzini, S., Fontaine, A., Giorgetti, Ch., Dartyge, E. & Kappler, J. P. (1998). *J. Appl. Phys.* **83**, 7291–7293.

Okane, T. *et al.* (2009). In preparation.

high pressure

Onodera, A., Nakai, Y., Kunitomi, N., Pringle, O. A., Smith, H. G., Nicklow, R. M., Moon, R. M., Amita, F., Yamamoto, N., Kawano, S., Achiwa, N. & Endo, Y. (1987). *Jpn. J. Appl. Phys.* **26**, 152–156.

Schütz, G., Wagner, W., Wilhelm, W., Kienle, P., Zeller, R., Frahm, R. & Materlik, G. (1987). *Phys. Rev. Lett.* **58**, 737–740.

Suzuki, M., Kawamura, N., Mizumaki, M., Urata, A., Maruyama, H., Goto, S. & Ishikawa, T. (1998). *Jpn. J. Appl. Phys.* **37**, L1488–L1490.

Syshchenko, O., Fujita, T., Sechovsk'y, V., DiviUs, M. & Fujii, H. (2001). *J. Alloys Compd.* **317–318**, 438–442.

Tanaka, H. *et al.* (2006). *J. Synchrotron Rad.* **13**, 378–391.

Wohlfarth, E. P. & Rhodes, P. (1962). *Philos. Mag.* **7**, 1817–1824.

Yabashi, M., Goto, S., Shimizu, Y., Tamasaku, K., Yamazaki, H., Yoda, Y., Suzuki, M., Ohishi, Y., Yamamoto, M. & Ishikawa, T. (2007). *AIP Conf. Proc.* **879**, 922–925.